Tailoring the microstructure, mechanical and tribological properties and oxidation resistance of (AlTiCrVTa)N_x coatings by controlling nitrogen content

Huan Luo[a], Hui Sun[b,*], Lizhi Yuan[c], Peipei Wang[a], Xing Zhao[a], Pascal Briois[d], Alain Billard[d]

[a]School of Materials Science and Engineering, Xi'an University of Science and Technology, Xi'an, 710054, China
[b]Shandong Key Laboratory of Optical Astronomy and Solar-Terrestrial Environment, School of Space Science and Physics, Shandong University, Weihai, Shandong,
264209, China
[c]Chuanqing Drilling Engineering Company Limited, Changqing Drilling Company, No.151 Fengcheng Fourth Road, Xi'an, 710018, China
[d]FEMTO-ST Institute (UMR CNRS 6174), UBFC/UTBM, Site de Montb´eliard, F-90010, Belfort, France

Corresponding authors : **huisun@sdu.edu.cn**

Abstract :

A set of novel (AlTiCrVTa)Nx coatings are synthesized by DC magnetron sputtering to methodically investigate the effect of nitrogen content on the microstructure, mechanical and tribological properties and oxidation behavior of the coatings for the first time. As the nitrogen content increases, the coating structure transitions from amorphous to a simple fcc structure, accompanied by a change of preferred orientation from (200) to (111) and an enhancement in crystallinity. The coating morphology changes from featureless glassy to columnar crystals. The highest nanohardness of 38.1 GPa and the best wear rate of 4.9×10^{-7} mm3/Nm are achieved at 43.3 at.% nitrogen content. The friction coefficient exhibits a downward trend with rising nitrogen content, reaching the lowest value of 0.47 at 49.8 at.% nitrogen content. The oxidation tests reveal that the oxidation resistance deteriorates with increasing nitrogen content, caused by the looser structure and large-sized grain boundaries.

Keywords : Microstructure, Mechanical and tribological properties, Magnetron sputtering, High-entropy nitride coatings

1.Introduction :

With the rapid development of the modern aviation industry, aircraft engines are facing harsh working environments with higher temperatures, higher pressures and higher loads [1,2]. Especially for aircraft operating in sandy and dusty environments, such as near desert and volcanic ash active areas, its compressor blades suffer from serious wear by solid particles [3,4]. It has become the main source of compressor failure, seriously limiting the operational reliability and service life of aero engines. Fortunately, researchers have found that using hard protective coatings is an effective strategy to combat wear damage [5,6]. It is demonstrated that the effective hard protective coatings are mainly binary transition metal carbides and nitrides (TMC/Ns), such as TiN, ZrN, and WC [7–9]. They can resist wear caused by plastic deformation when impact occurs due to the outstanding hardness provided by the strong covalent bonds and nanocomposite structures. However, such TMC/Ns are insufficient to resist oxidative damage at higher temperatures which is the environmental condition that compressor blades have to face [10]. High-temperature oxidation would severely degrade the mechanical properties and wear resistance of binary TMC/Ns. Therefore, the oxidation resistance of hard protective coatings needs to be improved. At the same time, the continuous advancement of engine development also puts forward higher requirements for the mechanical properties and wear resistance of the hard protective coating required for compressor blades. Recently, with the explosive growth of research related to high-entropy alloys [11–13], high-entropy design concepts have profoundly stimulated the latest development of high-entropy ceramic coatings [14, 15]. The design and preparation of high-entropy ceramic coatings have therefore begun to attract widespread attention. Among them, high-entropy nitride coatings have excellent mechanical properties [16, 17], thermal stability [18], and corrosion resistance [19], making them a promising alternative to traditional hard protective coatings. For instance, Li et al. designed and fabricated $(MoSiTiVZr)N_x$ coating through reactive DC magnetron sputtering and demonstrated that the ultra-high hardness of 45.6 GPa can be reached at a nitrogen content of 53.7 at.% [20]. Xu et al. synthesized $(AlCrTiVZr)N_x$ films using HiPIMS technology by controlling nitrogen flow. The results pointed out that the coating deposited at the nitrogen flow rate of 12 cm has a super-hardness of 41.8 GPa and the lowest wear rate of 2.3×10^{-7} mm3/Nm [21]. Moreover, high-entropy nitride coatings also exhibit better anti-oxidation properties compared to corresponding traditional binary nitride coatings. Wang et al. conducted an in-depth study on the oxidation behavior of Al–Cr–Nb–Si–Zr high-entropy nitride coating at 850◦C in air atmosphere. The oxide scale with a multi-layer structure consisting of $Al_2O_3/Cr_2O_3/Al_2O_3$ with dispersed nanocrystalline ZrO_2 was proven to play a key antioxidant role [22]. The research results of Shen et al. [23] confirmed that the oxidation resistance of $(Al_{0.34}Cr_{0.22}Nb_{0.11}Si_{0.11}Ti_{0.22})N$ coating is superior to reported nitride coatings, and revealed that such excellent oxidation resistance is owing to the dense Al_2O_3 layer and inner Si-rich amorphous network.

In summary, the rational selection of multiple components to design high-entropy nitride coatings has great potential for the development of high-performance hard protective coatings that could meet stringent requirements. In the present work, we focus on a new group of high-entropy components Al, Ti, Cr, V and Ta, which have not been reported so far to the best of our knowledge. A series of novel $(AlTiCrVTa)N_x$ coatings with controllable nitrogen content are successfully prepared by magnetron sputtering with a multi-target configuration. The evolution trends of the coating's microstructure and growth morphology with nitrogen content are explored in detail. The mechanical properties, tribological performance and high-temperature oxidation behavior of the coatings are systematically studied. On these bases, the correlation between the nitrogen content, microstructure and various properties of the coating, as well as the corresponding mechanisms are explored in detail.

2. Coating deposition and Characterization

2.1 Coating preparation

The deposition of (AlTiCrVTa)Nx coatings was achieved through reactive DC magnetron sputtering technique using AlTi and CrV alloy targets, and Ta metallic target (Ø _300 mm × 6 mm, purity 99.9 at. %, respectively) in argon-nitrogen gas mixtures. The schematic diagram of the multi-target magnetron sputtering system is presented in Fig. 1. To ensure coating purity, the chamber was evacuated by mechanical pump and turbomolecular pump to below 10^{-5} mbar before deposition. The chamber employs three circular planar with water-cooled magnetron sputtering sources while the distance between the rotating substrate stage and the cathode is 90 mm. The AlTi and CrV cathodes were powered a by pulsed DC advanced energy dual generator and the Ta cathode was performed employing a DC generator. The chemical compositions of the coating were controlled by adjusting the discharge power of each target. The sputtering pressure was measured with an MKS Baratron gauge, while the gas flow rates were controlled by Brooks flowmeters. The silicon wafer, iron sheet, cemented carbide M2 and stainless steel slide were selected as the substrates to meet the needs of different tests, such as structure, residual stress, mechanical properties, tribological performance and anti-oxidation behavior. Before placing the substrate into the reactor, the substrates were cleaned with alcohol and acetone and dried with air, and then placed on a substrate holder at a fixed distance of 90 mm from the cathode surface to prevent any lateral microstructural gradients [24]. The substrates were unbiased and did not undergo any additional heating during the entire coating deposition process. The specific discharge parameters concerning the sputtering process are presented in Table 1. Besides, to enhance the adhesion between the high-entropy nitride coating and the substrate, the ion cleaning for the substrate powered by an RF power supply with the power of 300 W and the pressure of 1.75 Pa was employed for 1 h. Following, a high-entropy alloy AlTiCrVTa buffer layer with a thickness of 200 nm was pre-deposited before the (AlTICrVTa)Nx coating, and its discharge parameters remained basically unchanged from those of the high entropy nitride.

2.2 Coatings characterizations

The structural characterization of the coating was performed by using a Bragg-Brentano XRD configuration using a BRUKER D8 focus diffractometer (Bruker AXS, Karlsruhe, Germany) with a Co X-ray source. For the morphology evaluation, the microscopic observations of the top surface and brittle fracture cross-section of the coating and determination of the coating thickness were performed by a JEOL JSM 7800F FESEM. Since the light element nitrogen is difficult to accurately measure by EDS, the composition depth profile of the coatings was carried out by using a GD-OES (GD-Profiler 2, HORIBA France SAS). The radio frequency method was used, while the discharge voltage of 550 V was applied and the high-purity argon was employed as the discharge gas. The emission lines selected during analysis (corresponding all of them to atomic transitions) were 396 nm for Al, 365 nm for Ti, 425 nm for Cr, 411 nm for V, 301 nm for Ta, 386 nm for Fe, and 149 nm for N. The voltage applied to the photomultiplier tubes (PMT) was optimized for each wavelength to obtain maximum sensitivity.

The residual stress and nanohardness of the coating were tested by the substrate curvature radius method and nanoindentation tester (CSM Instruments), respectively. The specific measurement details can be found in previous work [25]. The tribological performance of the coating was measured via a pin-on-disk Tribometer (CSM, Switzerland). The test environment is the non-lubricated state against a 6 mm WC/Co ball in ambient air with a relative humidity of approximately 36%. Other test parameters were set as a normal load of 5 N, a sliding speed of 10 cm/s, a contact track radius of 3 mm, and 10,000 sliding cycles. After the tribological test, the cross-sectional profile of the wear track was characterized by an Altysurf profilometer (Altisurf 500), manufactured by Altimet, equipped with a tungsten micro force inductive probe allowing an accuracy of about 20 nm. Before each measurement, the experimental device was calibrated using reference sample number 787,569. The normalized wear rate (Wr) was calculated based on the formula Wr =V/(L × S), in which V is the wear volume, L is the applied normal load, and S is the sliding distance. The morphology and elemental analysis of the wear track were completed by SEM/EDS. The oxidation resistance of the coating was tested by annealing treatment in an air atmosphere at different temperatures (from 200 ◦C up to 800 ◦C with an incremental step of 100 ◦C) in the furnace of Nabertherm. During the annealing treatment, the heating rate was set to 100 ◦C/h, and after achieving the preset temperature the dwell time was fixed at 2 h. After the heat preservation is completed, all samples were naturally cooled in the furnace until reaching room temperature. Here, note that the cyclic oxidation test was employed in the present work. Each sample underwent oxidation sequentially at each temperature from 200 ◦C to 800 ◦C (2 h dwell time at each temperature). Following, XRD and

SEM/EDS (Bruker Nano, Berlin, Germany) were employed to determine the development of oxidation degree and oxidation products.

3 Results and discussion

3.1 Chemical composition and residual stress

The chemical composition characterized by GD-OES and residual stresses of the (AlTiCrVTa)Nx coatings with varying nitrogen contents are given in Table 2. Benefiting from the precise control during the coating preparation, the relative concentration of five metal elements at the cationic sites of the coating is almost one-fifth, which is highly consistent with the design criteria of high-entropy engineering. While controlling the equiatomic concentration ratio of metal elements, the nitrogen content is increased from 25.6 at.% to 49.8 at.% by regulating the introduced nitrogen flux. It shows a tendency toward nitrogen saturation but remains substoichiometric from 0.34 to 0.99 for all high-entropy (AlTiCrVTa)Nx coatings.

The chemical composition profile as a function of coating thickness for all (AlTiCrVTa)Nx coatings is depicted in Fig. 2. Clearly, the concentration of each element remains stable along the coating depth, indicating a homogeneity distribution of elements through the coating thickness. The relative concentrations of all metal elements are equiatomic, while the nitrogen content is about 25.6, 31.9, 37.2, 43.3, 47.1 and 49.8 at.%, respectively. This homogeneous composition depth profile is because the (AlTiCrVTa)N_x coatings are not disturbed by abnormal changes in discharge parameters caused by the target poisoning during coating growth process, which has a significant impact on the concentration uniformity of each element in the coatings [26]. It is attributed to real-time automatic regulation of nitrogen flux during coating deposition, which is achieved through OES monitoring of the plasma above the AlTi target and subsequent automatic feedback adjustment of the N2 flow rate (to maintain the stability of plasma chemical reaction). In addition, Table 2 shows the residual stress of the (AlTiCrVTa)N_x coating. One can observe that all coatings fall within the compressive stress range and increase from 0.84 GPa at 25.6 at.% nitrogen content to 3.93 GPa at 49.8 at.% nitrogen content. Since (AlTiCrVTa)N_x coating preparation in the present work did not employ assisted heating, this progressive accumulation of compressive stress is inferred to originate primarily from the increase in bombardment energy of coating-forming particles caused by the introduction of more nitrogen into the plasma. The speculation of increased bombardment energy is also supported by the transition of the preferred orientation of the diffraction peaks reflected by subsequent XRD.

3.2 Microstructure and morpholopgy

Fig. 3 shows the X-ray diffraction spectra of (AlTiCrVTa)N_x coatings with nitrogen varying from 25.6 to 49.8 at.%. At lower nitrogen contents of 25.6 at.% and 31.9 at.%, the coatings exhibit an amorphous structure. The only identifiable signal peak present at 52.2° _is attributed to substrate M2. It is attributed to the fact that the lattice distortion and slow diffusion effects induced by the mutual solubility of the five principal elements weaken the driving force required for the transition from amorphous to crystalline configuration and slow down the crystallization kinetics. The lower concentration of nitrogen atoms contained in the (AlTiCrVTa)N_x coating is not enough to overcome them and facilitate the establishment of the lattice, thus maintaining the amorphous structure. When the nitrogen content rises to 37.2 at.%, the amorphous structured spectrum splits into two broad peaks corresponding to the (111) and (200) of NaCl-type fcc structure. This is consistent with the structure of TiN, CrN or VN, suggesting that the development of the nitrides with fcc structure is initiated, but accompanied by insufficient crystallinity. As the nitrogen content continues to increase from 43.3 at. % to 49.8 at.%, the coatings display a well-defined NaCl-type fcc structure marked by the intense fcc-(111) and (200) diffraction peaks, which is because higher nitrogen concentrations effectively strengthen the lattice order and promote nitride formation. Combined with the coating chemical compositions shown in Table 2, the formation of simple fcc-structured high-entropy nitride coatings within the nitrogen content interval from 37.2 at.% to 49.3 at.% is determined. The key role of mutual solubility driven by the high entropy effect resulting from multiple equiatomic principal elements on the formation and stabilization of the simple phase is also confirmed [27]. Regarding the nitrides of the five principal metals, i.e., Al, Ti, Cr, V and Ta, selected in the present work, except AlN that has an hcp structure other nitrides (TiN, CrN, VN and TaN) all have NaCl fcc structures. Under this condition, the (AlTiCrVTa)Nx coating is believed to tend to grow into a NaCl fcc structure in which Al, Ti, Cr, V and Ta atoms are randomly distributed on the metal sublattice. Similar results for high-entropy nitride coatings with fcc structures instead of multiple binary nitride structures have also been reported in previous works for AlCrNbSiTiN coating [28] and (CrNbTiAlV)Nx coating [29].

In addition to the nitridation-induced transformation from amorphous to fcc structure, the diffraction peaks of four coatings with nitrogen content from 37.2 at.% to 49.8 at.% exhibit sustained low-angle shifts and preferred orientation transitions from (200) to (111). The low-angle shift of the diffraction peak corresponding to the increasing average lattice constant (shown in Fig. 3 (b)) is driven by the expansion of interplanar spacing caused by the continuous incorporation of N atoms and the amassing defects within the coatings induced by the stronger bombardment effect. In terms of the preferred orientation evolution, from the thermodynamic perspective, it is determined by the growth competition between different crystal planes driven by the minimization of the total system energy [30]. It is known that the accumulated strain in the coating is strongly dependent on the energy and flux of bombarding particles reaching the growing coating. At a low nitrogen content of 37.2 at.%, that is, at the plasma formed by a low nitrogen flow rate, the bombarding flux of coating-forming particles is smaller, resulting in a low-strain state. Under this condition, the surface energy accounts for a larger proportion of the total energy in the coating system, which drives the (200) orientation that possesses the lowest surface energy to grow preferentially. At higher nitrogen content from 43.3 at.% to 49.3 at.%, the stronger average bombarding energy supported by the higher flux of bombarding particles promotes the strain energy instead of surface energy to develop to become dominant. Therefore, the (111) plane with the lowest strain energy grows faster and becomes the preferred orientation. Besides, the grain size variation trend (calculated from Scherrer’s formula based on FWHM) of (AlTiCrVTa)Nx coatings with varying nitrogen content is listed in Table 2. One can observe that the grain size gradually coarsens with nitrogen content, which is provided by the thermal effect caused by the enhanced total energy of bombardment experienced by the growing coating. This inducement for promoting grain coarsening is consistent with the driving force for the preferred orientation transition, namely the enhanced bombardment energy with nitrogen content. Fig. 4 presents the cross-section and top surface morphologies of (AlTiCrVTa) Nx coatings with different nitrogen content. Initially, the coating presents a dense glassy amorphous cross-section and a smooth top surface at the low nitrogen content of 25.6 at.%. This is the common morphology of high-entropy alloy coatings without nitrogen [31]. As the nitrogen content reaches 31.9 at.%, the amorphous morphology remains in the cross-section, while the corresponding top surface transforms into dome-shaped particles with fine dimensions under magnification. With the increase of nitrogen content to 37.2 at.%, the glass-like and featureless morphology is replaced by columnar structure, indicating the formation of nanograins, and is highly consistent with the XRD results. Meanwhile, the granular particles on the top surface grow substantially. For the coating with 43.3 at.% nitrogen content, the typical dense and fine columnar crystals appear in the cross-section. The top surface becomes quite denser and has a smooth topography. Both are contributed by enhanced crystallinity driven by higher average bombardment energy and appropriate nitrogen content. As the nitrogen content further increases, the increase in the lateral size of columnar crystals on the cross-section is discernible.

The column boundaries become distinct and even some micro-voids between columns are distinguished as well. The size of the spherical particles that are irregularly stacked on the top surface increases accordingly. All these features are attributed to the coalescence and coarsening events of the grains under strong bombardment effects. To sum up, judging from the overall evolution trend, the transformation process of coating morphology with nitrogen content is consistent with the XRD results.

3.3 Mechanical properties

Fig. 5(a) displays the hardness and Young's modulus of (AlTiCrVTa) Nx coatings as a function of nitrogen content, such that nitrogen content significantly modulates the mechanical properties of the coating. Through the increase of the nitrogen content from 25.6 at.% to 43.3 at. %, the hardness and Young's modulus show an obvious upward trend. The highest hardness of 38.1 GPa and Young's modulus of 359.8 GPa are achieved at 43.3 at.% nitrogen content. Beyond this content, the hardness and Young's modulus display a deteriorating trend, reaching 25.6 GPa and 288.6 GPa, respectively. At nitrogen levels from 25.6 at.% to 43.3 at.%, the strengthening of covalent bonds caused by nitride formation and increase as well as lattice distortion associated with the incorporation of more nitrogen atoms are responsible for this measured hardness rises. On the one hand, covalently bonded nitride is gradually formed with the incorporation of nitrogen, which gives the coating greater strength. Moreover, as the nitrogen content increases, the crystallization of nitride continues to occur and the strong covalent bondings between nitrogen atoms and metal atoms increase in number, thus causing the coating to harden. On the other hand, five transition metal atoms and nitrogen atoms, which have obvious differences in atomic radius and electronegativity, are randomly distributed on the lattice sites of the (AlTiCrVTa)Nx coatings. There thus must be lattice distortion and subsequent local lattice strain [32,33]. This lattice strain field may get much more severe with the incorporation of nitrogen content, thereby increasing the energy threshold required for the onset of dislocation slip, resulting in significant solid-solution strengthening. Of additional importance are the compressive stress and (111) preferred orientation, both of which also contribute to the increase of hardness in this nitrogen content interval. The compressive stress could hinder plastic flow during deformation [34], while the (111) orientation is the hardest orientation often observed in fcc-structured nitride due to the geometrical strengthening [35], thus leading to an overall increase in the coating's resistance to plastic deformation. When the nitrogen content increases from 43.3 at.% to 49.8 at.%, the grain size increases from 22.2 nm to 28.1 nm (in Table 2), resulting in a drop in hardness due to the Hall-Petch effect. Meanwhile, the loose columnar crystal structure (in Fig. 4(f)) is insufficient to provide effective resistance to plastic deformation, thus also causing the coating to soften. Here, although the hardening contributions provided by covalent bonding, lattice distortion as well as compressive stress are still present, they may fail in competition with the softening effect resulted from grain coarsening and loose structure, thus resulting in a reduction in hardness finally.

Based on the obtained values of hardness and Young's modulus, the ratios H/E and H3/E2, indicating the material's resistance to elastic deformation and its ability to dissipate energy at plastic deformation during loading [36], are plotted in Fig. 5(b). Similarly, they show the same evolution trend as hardness and Young's modulus with increasing nitrogen content. The H/E ratio could be used as a predictive parameter for material wear resistance whether in bulk or coating form, and its effectiveness will be validated in the following section.

3.4 Tribological performance

The dynamic friction curves of (AlTiCrVTa)N_x coatings as a function of sliding cycles and the average coefficient of friction (COF) are presented in Fig. 6(a), while the calculated wear rates of (AlTiCrVTa)N_x coatings with varying nitrogen content are depicted in Fig. 6(b).

Since the coatings with low nitrogen content of 25.6 at.% and 31.9 at.% are severely damaged during tribological testing, manifested by large-scale spalling and wear-through of wear tracks, their COF and wear rate values cannot be accurately obtained. Therefore, the COF and wear rate of these two coatings are not given in Fig. 6.

From Fig. 6, except for the coating with 37.2 at.% nitrogen content in which the friction curve transitions to the steady state more slowly, the dynamic friction curves of all coatings show similar evolution features. That is, the friction coefficient increases rapidly at the initial running-in stage and then enters the steady wear stage after about 2000 laps. In addition, the dynamic friction curve of the coating with the highest nitrogen content 49.8 at.% has the most dramatic fluctuations compared to that of the other coatings, evidenced by the more obvious burrs on it. This is most likely related to the wear type, which will be revealed later in conjunction with the wear rate and wear track morphology. By extracting the steady state values, the average COF value is determined and given adjacent to each dynamic curve in Fig. 6 (a). It can be seen that as the nitrogen content increases, the COF value shows a decreasing trend, from 0.68, 0.53, 0.51 to 0.47 corresponding to the nitrogen content from 37.2, 43.3, 47.1 to 49.8 at.%, respectively. It indicates that the increase in nitrogen content is beneficial to the antifriction capability of (AlTiCrVTa)Nx high-entropy nitride coatings.

Fig. 6(b) shows the wear rate of the (AlTiCrVTa)Nx coating as a function of nitrogen content. Apparently, except for the coating with the highest nitrogen content, the wear rates of the other coatings show a trend consistent with the mechanical properties. From 37.2 to 43.3 at.% nitrogen content, the wear rate decreases and obtains a minimum value of 4.9×10^{-7} mm3/Nm, where the coating has the best mechanical properties. As the nitrogen content increases, the wear rate increases to 3.1×10^{-6} mm3/Nm, caused by the reduced mechanical properties. However, when the nitrogen content reaches 49.8 at.%, the wear rate decreases again inversely, although here the mechanical properties of the coating are insufficient. It is thus inferred that such variation is synergistically promoted by high compressive stress and minimum friction coefficient.

To reveal the above-mentioned tribological performance and underlying mechanism, the SEM morphology and surface element mapping of the wear track of (AlTiCrVTa)Nx coating are given in Fig. 7. The coatings with nitrogen contents of 25.6 and 31.9 at.% are severely damaged (Fig. 7(a) and (b)). The wear tracks show extensive spalling and exposure of the underlying M2 steel, which is marked by the green area in the EDS surface mapping. This is because of the low hardness, poor damage tolerance (characterized by the H/E value [20]) and high friction coefficient that makes the coating difficult to resist plastic deformation and brittle fracture. For the coating with 37.2 at.% nitrogen content, the wear track remains complete, and no flake peeling occurs, implying significantly enhanced wear resistance (Fig. 7(c)). Obvious grooves and accumulation of wear debris as well as black adhesive material, indicated by white arrows, in the middle and edges of the wear track can also be observed, which means the mixed wear mode of adhesive and abrasive [37]. At 43.3 at.% nitrogen content (Fig. 7(d)), the wear track becomes narrowest, shallowest, and smoothest among all coatings. Only some wear debris remains while the grooves and scratches formed by ploughing are not visible, corresponding to the best wear resistance. It is contributed by optimal mechanical properties, increased compressive stress and lower friction coefficient at 43.3 at.% nitrogen content.

As the nitrogen content increases to 47.1 at.% (Fig. 7(e)), there are massive adhesion materials evidenced by the obviously black flake oxides. It confirms the existence of tribo-layer, as occurs in the two coatings with lower nitrogen content of 37.2 and 43.3 at.%. Furthermore, it is also found that the increase in nitrogen content from 25.6 at.% to 47.1 at.% makes the wear track smoother, which is consistent with the monotonic decrease in the friction coefficient. For the coating with 49.8 at.% nitrogen content, the wear appears to be getting more severe than that with lower nitrogen. A large amount of wear debris and massive grooves are observed, representing typical abrasive wear. This wear mode is caused by insufficient hardness, which makes the coating surface difficult to resist plastic scratching by abrasive particles during multiple cyclic friction processes [38]. However, despite the apparent increase in grooves and scratches, its deteriorating effect on the wear resistance of the coating is not present, as confirmed by the calculated reduced wear rate value. Furthermore, this morphology and abrasion wear mode are also inferred to be the origin of dramatic fluctuations in the dynamic friction curve ofthe coating with 49.8 at.% nitrogen content (as shown in Fig. 6(a)).

3.5 Oxidation resistance

The (AlTiCrVTa)Nx coatings are tested at 600, 700 and 800 ◦C in an air environment for 2 h to evaluate the coating oxidation resistance. After the oxidation test, the phase structure, oxidation products, and cross-sectional morphologies of the (AlTiCrVTa)Nx coatings are characterized. It can be seen from the XRD results that the phase structure of the coating maintains a simple fcc structure after oxidation at 600 ◦C, as that of as-deposited coatings, suggesting the oxidation reaction of all (AlTiCrVTa)Nx coatings is not activated at 600 ◦C. However, upon oxidation at 700 ◦C, the simple fcc structure of all (AlTiCrVTa)Nx coatings is destroyed, as shown in Fig. 8, indicating that the oxidation reaction occurs on a large scale. When the oxidation temperature is further increased to 800 ◦C, all (AlTiCrVTa)Nx coatings are completely oxidized regardless of the nitrogen content, and some coatings even experience extensive chalking and flaking.

Fig. 8 presents the X-ray diffraction pattern of (AlTiCrVTa)Nx coatings with various nitrogen contents after oxidation test at 700 ◦C in air. For all (AlTiCrVTa)Nx coatings, the crystalline oxide peaks become dominant and are classified as the rutile TiO2 phase (ICDD PDF#21- 1276). Two coatings with nitrogen content of 43.3 and 47.1 at.% can be detected with a weak fcc-(111) peak, which represents the coexistence of high-entropy nitride and oxide phases. However, it should be noted that for (AlTiCrVTa)Nx coatings with lower nitrogen content, the absence of fcc diffraction peaks does not mean that the coating has been fully oxidized and exhausted. Since the structures of (AlTiCrVTa)Nx coatings with low nitrogen content from 25.6 to 37.2 at.% are amorphous and nanocrystalline, they are difficult to be resolved on the diffraction spectra after the appearance of a high-intensity crystalline oxide peaks. Therefore, it is difficult to determine the effect of nitrogen content on the oxidation resistance of (AlTiCrVTa)Nx coatings only through XRD results. Further detailed analysis needs to be carried out through SEM/EDS.

In order to characterize more structural details of the coating and its oxide scale, the (AlTiCrVTa)Nx coatings after oxidation test at 700 ◦C are brittlely broken. The cross-sectional SEM micrographs and corresponding EDS mappings of each coating are displayed in Fig. 9. For the three coatings with 25.6, 31.9 and 37.2 at.% nitrogen content, the thickness of the oxide scale formed during the oxidation process is approximately the same, about 72% of the total thickness of the coating. Further increases in nitrogen content yield a thicker oxide scale. As the nitrogen content rises from 43.3 at.% to 49.8 at.%, the thickness of the oxide scale increases until the coating is completely oxidized. This overall thickening trend of the oxide scale confirms that the antioxidant capacity of (AlTiCrVTa)Nx coating deteriorates with the increase in nitrogen content. The reason for this deterioration in oxidation resistance with nitrogen content includes two aspects. On the one hand, the coating density changes significantly with nitrogen content, as confirmed by SEM morphologies in Fig. 4. The coatings with lower nitrogen content present denser structures with fewer micropores. By contrast, significant intra- and inter-column porosities and micro-defects are observed in the coatings with higher nitrogen content. Such a looser structure enriches the channels and micropores for oxygen transmission, therefore weaker antioxidant properties can be expected. On the other hand, as the nitrogen content increases, the grain size of (AlTiCrVTa)Nx coating gradually coarsens, and thus the accompanying grain boundaries provide shorter and smoother channels for oxygen intradiffusion transporting. Consequently, the oxygen barrier ability of the coating gradually deteriorates with the nitrogen content. Besides, it is found that there is an orientation dependence between the (AlTiCrVTa)Nx coating and the oxide scale formed on it. As marked in Fig. 8, at low nitrogen content from 25.6 to 37.2 at.%, the growth of TiO_2(110) is promoted, corresponding to amorphous and fcc(200) of the as-deposited coating. Differently, at high nitrogen content from 43.3 to 49.8 at.%, the growth of TiO2(200) is preferential, corresponding to the amorphous and fcc (111) of the as-deposited coating. However, its effect on antioxidant properties is very limited.

Generally, in addition to the density and grain boundary volume of the coating, the oxidation resistance of the coating is also associated with the characteristics of the oxide scale formed after selective oxidation of specific elements. Detailed observation of SEM cross-sectional morphologies in Fig. 9 reveals that the oxide scale of (AlTiCrVTa)Nx coating is composed of two distinct layers. They are respectively a glassy outer layer with a thickness of hundreds of nanometers and a loose oxide highlighted by the yellow dotted box in Fig. 9. To explore the two-layer structure of the oxide scale, the cross-sectional EDS mappings of each element for two (AlTiCrVTa)Nx coatings with 37.2 and 49.8 at.% nitrogen content are shown as representative in Fig. 10. According to the difference in element distribution in EDS mappings, two distinct regions are perceived and labeled as Region I and Region II. Obviously, the high concentration of Al element is concentrated in Region I, marked by the blue. Meanwhile, this narrow region is also enriched in O elements and trace amounts of Ti, Cr, V and Ta elements. Therefore, it is inferred that the outermost layer of the oxide scale is Al_2O_3. This is due to the occurrence of Al segregation at high temperatures. Region II is composed of uniform and high concentrations of Ti, Cr, V, Ta and O elements, and the inner layer of the oxide scale is judged to be a mixture of TiO_2 and oxides of other principal metal elements. Among them, the rutile TiO2 structure is clearly confirmed by XRD. Although other metal oxides are not explicitly verified by XRD, they may have formed because they have more negative formation enthalpies than the corresponding nitrides (given in Table 3 [39,40]). Possibly due to smaller content or amorphous structure, other metal oxides are not detected by diffraction technique. Therefore, it can be concluded that the oxide scale formed on the (AlTiCrVTa)Nx coating during the high-temperature oxidation process is a double-layer structure consisting of an Al_2O_3 outmost layer followed by a rutile TiO2 layer accompanied by oxides of other metal elements. The formation of this oxide scale is supported by the outward migration of Al and the inward diffusion of oxygen provided by the grain boundaries and intercolumn gaps. The diffusion resistance and antioxidant capabilities of this oxide scale can impart a higher onset oxidation temperature to (AlTiCrVTa)Nx coatings than corresponding binary nitrides or Al-containing nitride coatings, such as TiN, TaN and TaAlN [41–43]. In summary, the key factors that promote the oxidation resistance of (AlTiCrVTa)Nx coating are the dense structure, the high-density grain boundaries provided by fine grains and the diffusion-resistant oxide scale.

4 Conclusion

High-entropy nitride coatings are promising alternatives to traditional nitride hard protective coatings due to their excellent mechanical properties, thermal stability and oxidation resistance. In the present work, a series of high-entropy nitride (AlTiCrVTa)Nx ($0.34 \leq x \leq 0.99$) coatings are designed and prepared by reactive DC magnetron sputtering. The effect of nitrogen content on the microstructure, growth morphology, residual stress, mechanical properties, tribological performances and oxidation behavior of the coatings is systematically investigated for the first time. Results regarding microstructure demonstrate that with the nitrogen content increases, the coating structure transitions from amorphous to simple NaCl fcc structure, accompanied by a change in preferred orientation from low-surface-energy (200) to low-strain-energy (111) and an enhanced crystallinity. The coating with 43.3 at.% nitrogen content possesses the highest nanohardness of 38.1 GPa and Young's modulus of 359.8 GPa. Tribological results demonstrate a decrease in friction coefficient with rising nitrogen content, obtaining the lowest value of 0.47 at the nitrogen content of 49.8 at.%. The best wear rate of 4.9×10^{-7} mm3/Nm is dominated by mechanical properties, which is achieved at 43.3 at.% nitrogen content. Oxidation results in air at 700 ◦C reveal that the oxide scale on (AlTiCrVTa)Nx coating is a double-layer structure consisting of an Al_2O_3 outmost layer followed by a rutile TiO_2 layer + oxides of other metal elements. The lower the nitrogen content, the stronger the antioxidant properties, mainly supported by the denser structure and high-density grain boundaries.

Acknowledgements

The authors thank the Natural Science Basic Research Plan in Shaanxi Province of China [2022JQ-551], the National Key R&D Program of China [2022YFB3706600, 2022YFE0123000], the National Natural Science Foundation of China [62004117], and the Natural Science Basic Research Plan in Shaanxi Province of China [2022JQ-354] for their financial support of this study.

References

[1] X. Zhang, Y. Chen, J. Hu, Recent advances in the development of aerospace materials, Prog. Aero. Sci. 97 (2018) 22–34, https://doi.org/10.1016/j. paerosci.2018.01.001.

[2] J.C. Williams, E.A. Starke Jr., Progress in structural materials for aerospace systems, Acta Mater. 51 (2003) 5775–5799, https://doi.org/10.1016/j. actamat.2003.08.023.

[3] P. Yang, W. Yue, J. Li, G. Bin, C. Li, Review of damage mechanism and protection of aero-engine blades based on impact properties, Eng. Fail. Anal. 140 (2022) 106570, https://doi.org/10.1016/j.engfailanal.2022.106570.

[4] W. Tabakoff, T. Wakeman, Test facility for material erosion at high temperature, ASTM Int. (1979) 123–135.

[5] A. Leyland, A. Matthews, On the significance of the H/E ratio in wear control: a nanocomposite coating approach to optimised tribological behaviour, Wear 246 (2000) 1–11, https://doi.org/10.1016/S0043-1648(00)00488-9.

[6] J. Alqallaf, N. Ali, J.A. Teixeira, A. Addali, Solid particle erosion behaviour and protective coatings for gas turbine compressor blades-A review, Processes 8 (2020) 984, https://doi.org/10.3390/pr8080984.

[7] M.F. Othman, A.R. Bushroa, W.N.R. Abdullah, Evaluation techniques and improvements of adhesion strength for TiN coating in tool applications: a review, J. Adhes. Sci. Technol. 29 (2015) 569–591, https://doi.org/10.1080/ 01694243.2014.997379.

[8] T. Kuznetsova, V. Lapitskaya, A. Khabarava, S. Chizhik, B. Warcholinski, A. Gilewicz, The influence of nitrogen on the morphology of ZrN coatings deposited by magnetron sputtering, Appl. Surf. Sci. 522 (2020) 146508, https:// doi.org/10.1016/j.apsusc.2020.146508.

[9] A. Bhatt, H. Attia, R. Vargas, V. Thomson, Wear mechanisms of WC coated and uncoated tools in finish turning of Inconel 718, Tribol. Int. 43 (2010) 1113–1121, https://doi.org/10.1016/j.triboint.2009.12.053.

[10] O. Berger, The correlation between structure, multifunctional properties and application of PVD MAX phase coatings. Part III. Multifunctional applications, Surf. Eng. 36 (2020) 303–325, https://doi.org/10.1080/02670844.2019.1656861.

[11] E.P. George, D. Raabe, R.O. Ritchie, High-entropy alloys, Nat. Rev. Mater. 4 (2019) 515–534, https://doi.org/10.1038/s41578-019-0121-4s.

[12] Y.F. Ye, Q. Wang, J. Lu, C.T. Liu, Y. Yang, High-entropy alloy: challenges and prospects, Mater. Today 19 (2016) 349–362, https://doi.org/10.1016/j. mattod.2015.11.026.

[13] A. Sharma, High entropy alloy coatings and technology, Coatings 11 (2021) 372, https://doi.org/10.3390/coatings11040372.

[14] P.H. Mayrhofer, A. Kirnbauer, P. Ertelthaler, C.M. Koller, High-entropy ceramic thin films; A case study on transition metal diborides, Sci. Rep. 149 (2018) 93–97, https://doi.org/10.1016/j.scriptamat.2018.02.008.

[15] X. Xu, X. Wang, S. Wu, L. Yan, T. Guo, K. Gao, A.A. Volinsky, Design of super-hard high-entropy ceramics coatings via machine learning, Ceram. Int. 48 (2022) 32064–32072, https://doi.org/10.1016/j.ceramint.2022.07.145.

[16] P.K. Huang, J.W. Yeh, Effects of nitrogen content on structure and mechanical properties of multi-element (AlCrNbSiTiV) N coating, Surf. Coating. Technol. 203 (2009) 1891–1896, https://doi.org/10.1016/j.surfcoat.2009.01.016.

[17] A.D. Pogrebnjak, I.V. Yakushchenko, O.V. Bondar, V.M. Beresnev, K. Oyoshi, O. M. Ivasishin, C. Kozak, Irradiation resistance, microstructure and mechanical properties of nanostructured (TiZrHfVNbTa) N coatings, J. Alloys Compd. 679 (2016) 155–163, https://doi.org/10.1016/j.jallcom.2016.04.064.

[18] S.A. Firstov, V.F. Gorban, N.I. Danilenko, M.V. Karpets, A.A. Andreev, E. S. Makarenko, Thermal stability of superhard nitride coatings from high-entropy multicomponent Ti-V-Zr-Nb-Hf alloy, Powder Metall. Met. C+_ _52 (2014) 560–566, https://doi.org/10.1007/s11106-014-9560-z.

[19] H.T. Hsueh, W.J. Shen, M.H. Tsai, J.W. Yeh, Effect of nitrogen content and substrate bias on mechanical and corrosion properties of high-entropy films (AlCrSiTiZr) 100-xNx, Surf. Coating. Technol. 206 (2012) 4106–4112, https://doi. org/10.1016/j.surfcoat.2012.03.096.

[20] J. Li, Y. Chen, Y. Zhao, X. Shi, S. Zhang, Super-hard (MoSiTiVZr) Nx high-entropy nitride coatings, J. Alloys Compd. 926 (2022) 166807, https://doi.org/10.1016/j. jallcom.2022.166807.

[21] Y. Xu, G. Li, Y. Xia, Synthesis and characterization of super-hard AlCrTiVZr high-entropy alloy nitride films deposited by HiPIMS, Appl. Surf. Sci. 523 (2020) 146529, https://doi.org/10.1016/j.apsusc.2020.146529.

[22] J.J. Wang, F.Y. Ouyang, Oxidation behavior of Al-Cr-Nb-Si-Zr high entropy nitride thin films at 850◦ _C, Corrosion Sci. 187 (2021) 109467, https://doi.org/10.1016/j. corsci.2021.109467.

[23] W.J. Shen, M.H. Tsai, K.Y. Tsai, C.C. Juan, C.W. Tsai, J.W. Yeh, Y.S. Chang, Superior oxidation resistance of (Al0.34Cr0.22Nb0.11Si0.11Ti0.22)50N50 high-entropy nitride, J. Electrochem. Soc. 160 (2013) C531, https://doi.org/10.1149/ 2.028311jes.

[24] E. Aubry, P. Miska, L. Gigleux, A. Mezin, V. Demange, A. Billard, Microstructural and photocatalytic properties distribution of TiO2 coatings reactively sputtered as a function of the substrate position relatively to the Ti target, Surf. Coating. Technol. 202 (2008) 4980–4985, https://doi.org/10.1016/j.surfcoat.2008.04.097.

[25] H. Luo, H. Sun, F. Gao, A. Billard, Mechanical properties, thermal stability and oxidation resistance of HfC/a-C: H films deposited by HiPIMS, J. Alloys Compd. 847 (2020) 156538, https://doi.org/10.1016/j.jallcom.2020.156538.

[26] J.T. Gudmundsson, Physics and technology of magnetron sputtering discharges, Plasma Sources Sci. Technol. 29 (2020) 113001, https://doi.org/10.1088/1361- 6595/abb7bd.

[27] M.H. Tsai, J.W. Yeh, High-entropy alloys: a critical review, Mater. Res. Lett. 2 (2014) 107–123, https://doi.org/10.1080/21663831.2014.912690.

[28] B.S. Lou, Y.C. Lin, J.W. Lee, Mechanical properties and corrosion resistance of AlCrNbSiTiN high entropy alloy nitride coatings, Coatings 13 (2023) 1724, https:// doi.org/10.3390/coatings13101724.

[29] C. Zhang, X. Lu, C. Wang, X. Sui, Y. Wang, H. Zhou, J. Hao, Tailoring the microstructure, mechanical and tribocorrosion performance of (CrNbTiAlV)Nx high-entropy nitride films by

controlling nitrogen flow, J. Mater. Sci. Technol. 107 (2022) 172–182, https://doi.org/10.1016/j.jmst.2021.08.032.

[30] J. Pelleg, L.Z. Zevin, S. Lungo, N. Croitoru, Reactive-sputter-deposited TiN films on glass substrates, Thin Solid Films 197 (1991) 117–128, https://doi.org/10.1016/ 0040-6090(91)90225-M.

[31] Y. Zhang, T.T. Zuo, Z. Tang, M.C. Gao, K.A. Dahmen, P.K. Liaw, Z.P. Lu, Microstructures and properties of high-entropy alloys, Prog. Mater. Sci. 61 (2014) 1–93, https://doi.org/10.1016/j.pmatsci.2013.10.001.

[32] C.H. Lai, S.J. Lin, J.W. Yeh, S.Y. Chang, Preparation and characterization of AlCrTaTiZr multi-element nitride coatings, Surf. Coating. Technol. 201 (2006) 3275–3280, https://doi.org/10.1016/j.surfcoat.2006.06.048.

[33] J.W. Yeh, Alloy design strategies and future trends in high-entropy alloys, JOM 65 (2013) 1759–1771, https://doi.org/10.1007/s11837-013-0761-6.

[34] M.H. Hsieh, M.H. Tsai, W.J. Shen, J.W. Yeh, Structure and properties of two Al-Cr- Nb-Si-Ti high-entropy nitride coatings, Surf. Coating. Technol. 221 (2013) 118–123, https://doi.org/10.1016/j.surfcoat.2013.01.036.

[35] D.C. Tsai, Z.C. Chang, B.H. Kuo, M.H. Shiao, S.Y. Chang, F.S. Shieu, Structural morphology and characterization of (AlCrMoTaTi) N coating deposited via magnetron sputtering, Appl. Surf. Sci. 282 (2013) 789–797, https://doi.org/ 10.1016/j.apsusc.2013.06.057.

[36] W.L. Lo, S.Y. Hsu, Y.C. Lin, S.Y. Tsai, Y.T. Lai, J.G. Duh, Improvement of high entropy alloy nitride coatings (AlCrNbSiTiMo) N on mechanical and high temperature tribological properties by tuning substrate bias, Surf. Coating. Technol. 401 (2020) 126247, https://doi.org/10.1016/j.surfcoat.2020.126247.

[37] X. Niu, G. Dong, S. Wei, Y. Wang, B. Wang, H. Tian, Effects of nitrogen flow rate on the microstructure and mechanical and tribological properties of TiAlN films prepared via reactive magnetron sputtering, Ceram. Int. 49 (2023) 19885–19894, https://doi.org/10.1016/j.ceramint.2023.03.108.

[38] S.Y. Hsu, Y.T. Lai, S.Y. Chang, S.Y. Tsai, J.G. Duh, Combinatorial synthesis of reactively co-sputtered high entropy nitride (HfNbTiVZr) N coatings: microstructure and mechanical properties, Surf. Coating. Technol. 442 (2022) 128564, https://doi.org/10.1016/j.surfcoat.2022.128564.

[39] Greenwood, Chemistry of elements, Sykepleien 55 (1968) 412, https://doi.org/ 10.1002/crat.2170200510.

[40] D.-I.B. Rumpf, Thermochemical data of pure substances. https://doi. org/10.1016/s0165-2427(96)05632-2, 1997.

[41] H.-Y. Chen, F.-H. Lu, Oxidation behavior of titanium nitride films, J. Vac. Sci. Technol. A Vac. Surface. Films 23 (2005) 1006–1009, https://doi.org/10.1116/ 1.1914815.

[42] Y.I. Chen, J.H. Lin, C.C. Chou, Oxidation resistance and mechanical properties of Ta-Al-N coatings, Surf. Coating. Technol. 303 (2016) 41–47, https://doi.org/ 10.1016/j.surfcoat.2016.03.022.

[43] Y.C. Chim, X.Z. Ding, X.T. Zeng, S. Zhang, Oxidation resistance of TiN, CrN, TiAlN and CrAlN coatings deposited by lateral rotating cathode arc, Thin Solid Films 517 (2009) 4845–4849, https://doi.org/10.1016/j.tsf.2009.03.038.

Figure captions

Fig. 1. The schematic diagram of multi-target magnetron sputtering system for the deposition of (AlTiCrVTa)Nx coating.

Fig. 2. GD-OES composition profiles of (AlTiCrVTa)N_x coatings with a varying nitrogen content of (a) 25.6, (b) 31.9, (c) 37.2, (d) 43.3, (e) 47.1, (f) 49.8 at.%.

Fig. 3. (a) XRD spectra and (b) average lattice constants of (AlTiCrVTa)N_x coatings as a function of nitrogen content.

Fig. 4. SEM cross-section and top surface morphologies of (AlTiCrVTa)Nx coatings with different nitrogen content (a) 25.6, (b) 31.9, (c) 37.2, (d) 43.3, (e) 47.1, (f) 49.8 at.%.

Fig. 5. (a) Hardness H and Young's modulus E and (b) ratios of H/E and H3/E2 for (AlTiCrVTa)Nx coatings with different nitrogen content.

Fig. 6. (a) The dynamic friction curve varied with sliding cycles and the average coefficient of friction, as well as (b) the wear rate of (AlTiCrVTa)N_x coatings as a function of nitrogen content.

Fig. 7. SEM images of wear track morphology and surface elements mapping of (AlTiCrVTa)Nx coatings as a function of nitrogen content at.%: (a) 25.6, (b) 31.9, (c) 37.2, (d) 43.3, (e) 47.1, (f) 49.8.

Fig. 8. X-ray diffraction pattern of (AlTiCrVTa)N_x coatings with various nitrogen contents after 700 ◦C oxidation test.

Fig. 9. Cross-sectional SEM micrographs and corresponding EDS mappings of (AlTiCrVTa)N_x coatings with various nitrogen contents after 700 ◦C oxidation test in air.

Fig. 10. The cross-sectional SEM micrographs and corresponding EDS mappings of each element for the (AlTiCrVTa)N_x coatings with 37.2 and 49.8 at.% nitrogen content after 700 ◦C oxidation.

Table 1 The discharge parameters for the deposition of (AlTiCrVTa)Nx coatings.

Ar flow rate (sccm)	200	Targets	AlTi	CrV	Ta
N_2 flow rate (sccm)	6 → 15	Current (A)	2.5	1.68	1.14
Total pressure (Pa)	~ 1.7	Voltage (V)	324 → 338	279 → 305	289 → 298
Runtime (h)	2	Power (W)	810 → 845	468 → 513	330 → 340

Table 2. The chemical compositions, grain sizes, stoichiometric ratio and residual stress of (AlTiCrVTa)Nx coatings.

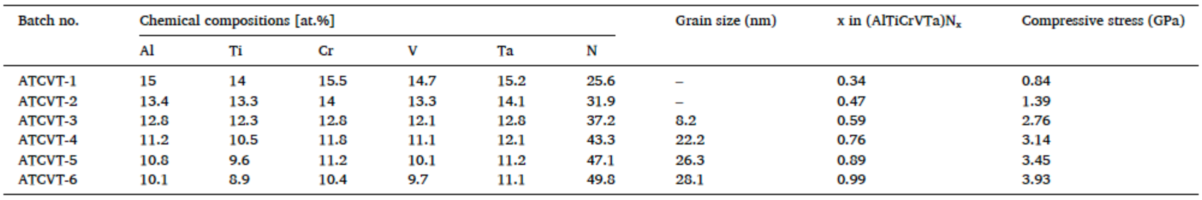

Batch no.	Chemical compositions [at.%]						Grain size (nm)	x in $(AlTiCrVTa)N_x$	Compressive stress (GPa)
	Al	Ti	Cr	V	Ta	N			
ATCVT-1	15	14	15.5	14.7	15.2	25.6	–	0.34	0.84
ATCVT-2	13.4	13.3	14	13.3	14.1	31.9	–	0.47	1.39
ATCVT-3	12.8	12.3	12.8	12.1	12.8	37.2	8.2	0.59	2.76
ATCVT-4	11.2	10.5	11.8	11.1	12.1	43.3	22.2	0.76	3.14
ATCVT-5	10.8	9.6	11.2	10.1	11.2	47.1	26.3	0.89	3.45
ATCVT-6	10.1	8.9	10.4	9.7	11.1	49.8	28.1	0.99	3.93

Table 3 The formation enthalpies ΔH (kj/per mole of metal element) of five binary nitrides and oxides based on the component elements of $(AlTiCrVTa)N_x$ coating.

	AlN	Al_2O_3	TiN	TiO_2	CrN	Cr_2O_3	VN	V_2O_5	TaN	Ta_2O_5
ΔH	-318.1	-837.9	-337.7	-944.0	-117.2	-570.0	-217.2	-775.0	-251.0	-1023.0

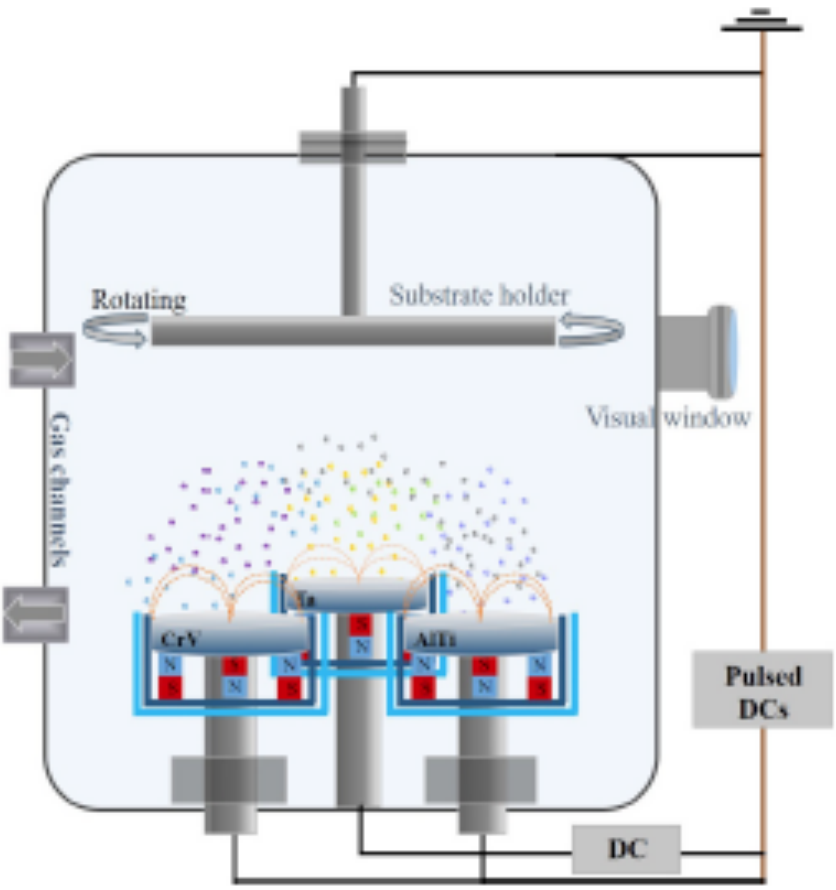

Figure 1

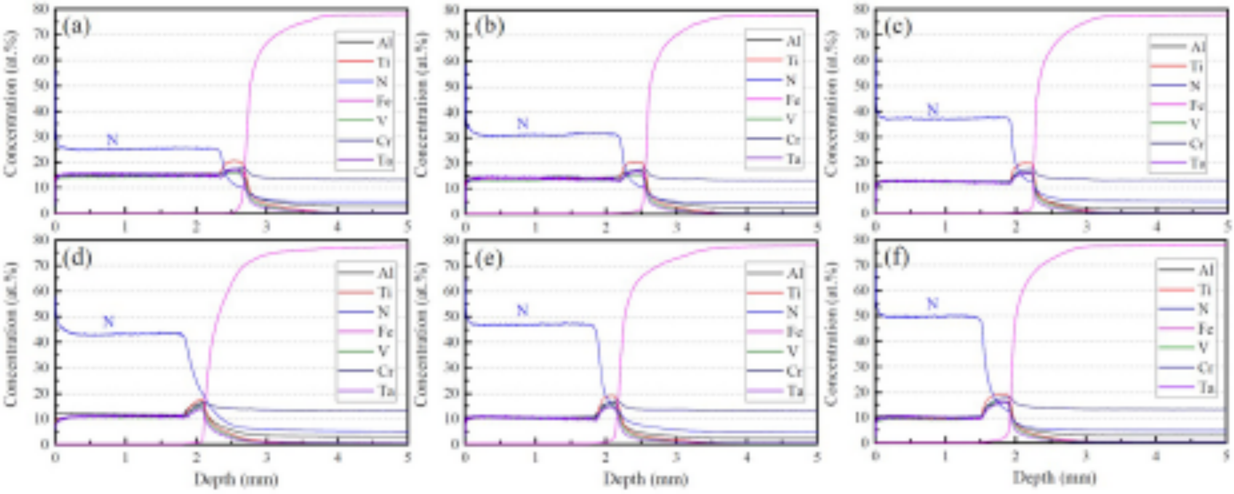

Figure 2

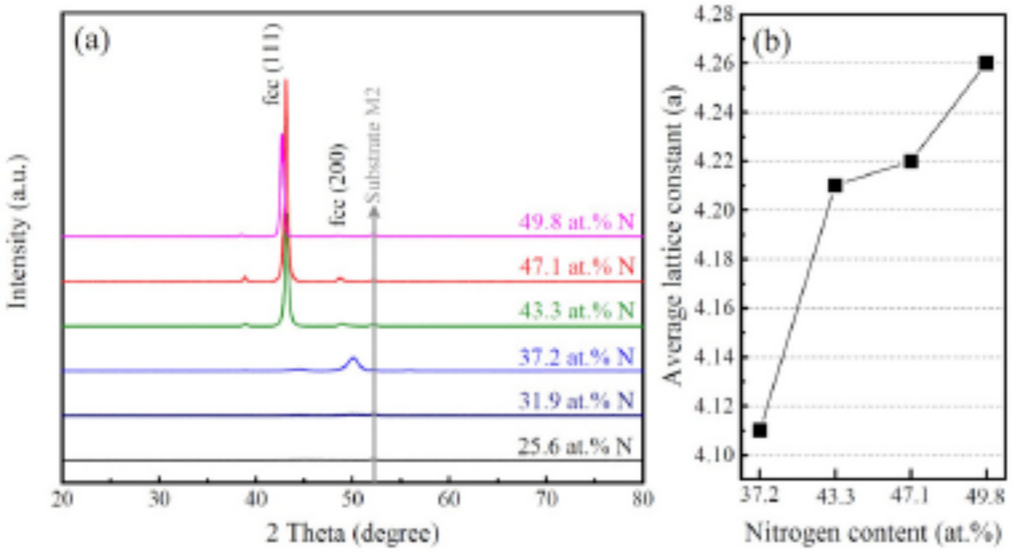

Figure 3

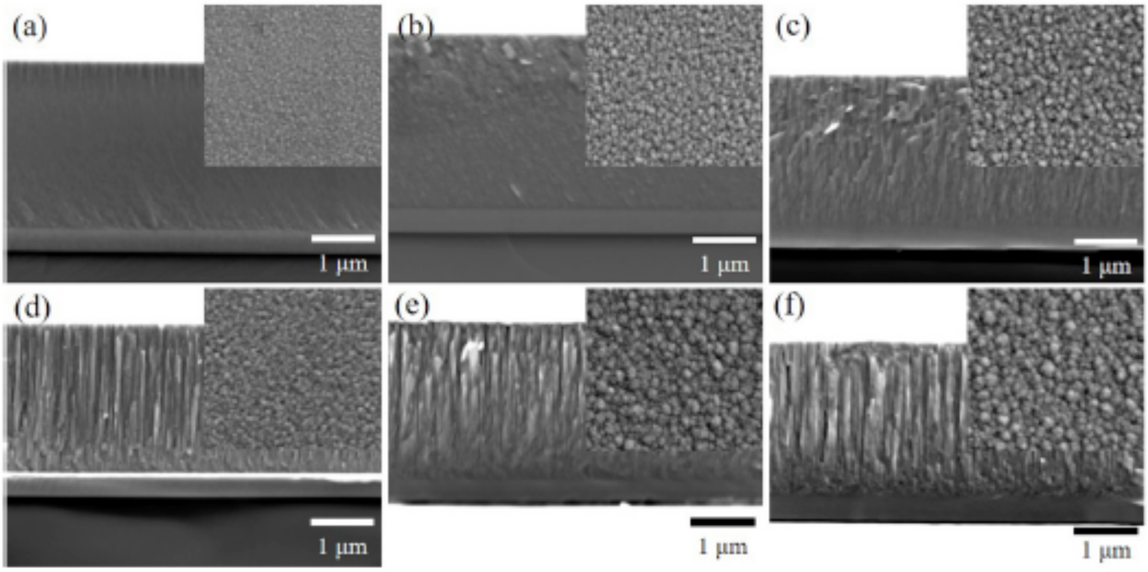

Figure 4

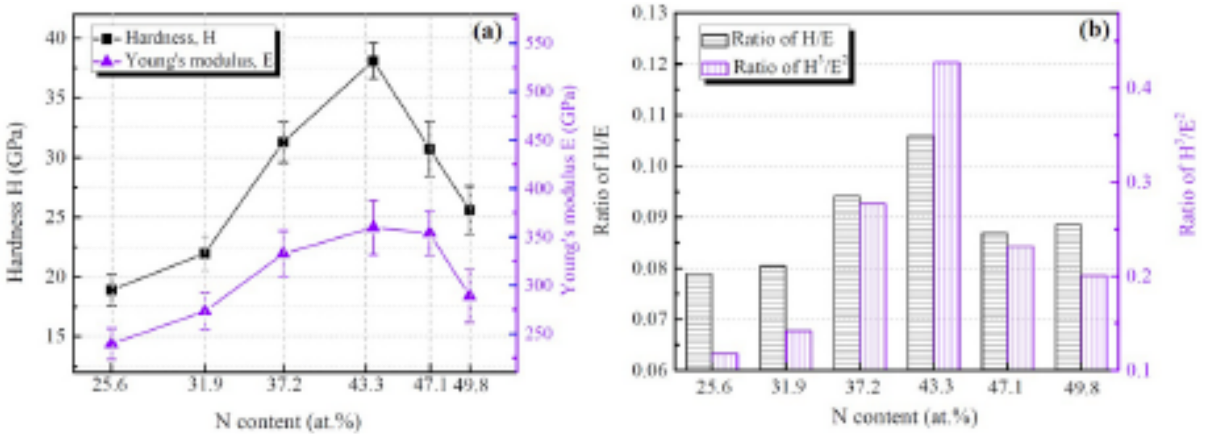

Figure 5

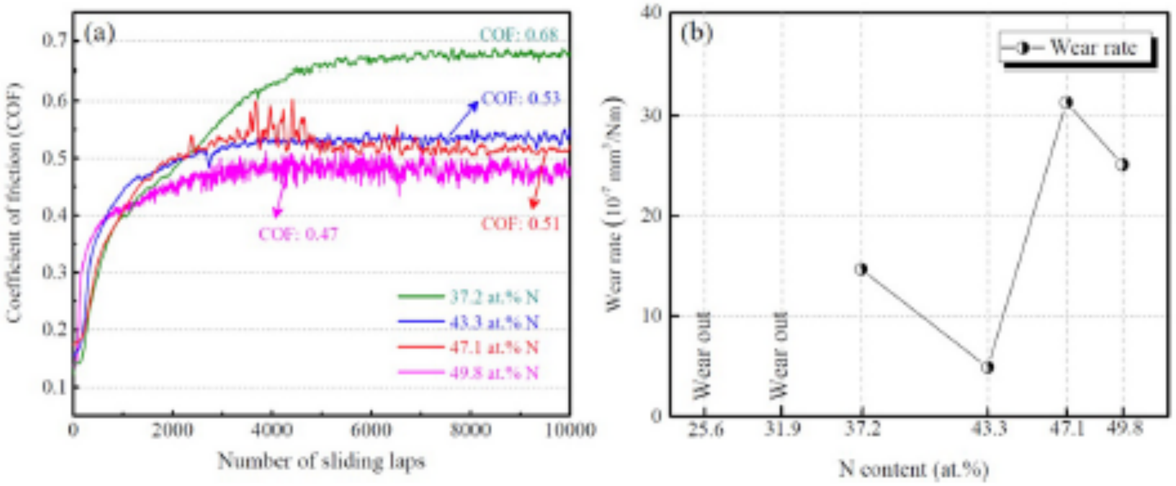

Figure 6

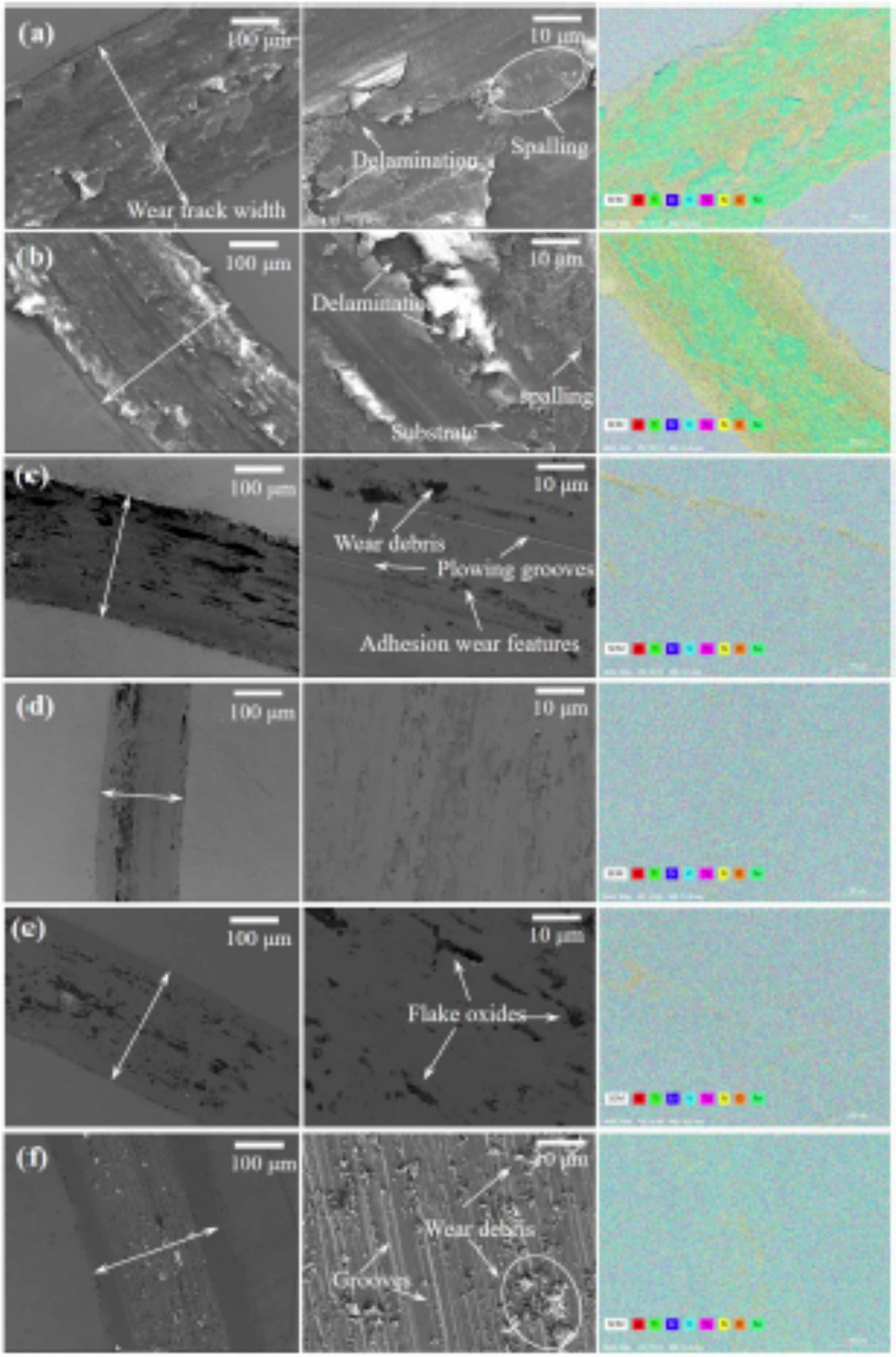
(a)
100 μm
10 μm
Wear track width
Delamination
Spalling
(b)
100 μm
10 μm
Delamination
spalling
Substrate
(c)
100 μm
10 μm
Wear debris
Plowing grooves
Adhesion wear features
(d)
100 μm
10 μm
(e)
100 μm
10 μm
Flake oxides
(f)
100 μm
10 μm
Wear debris
Grooves

Figure 7

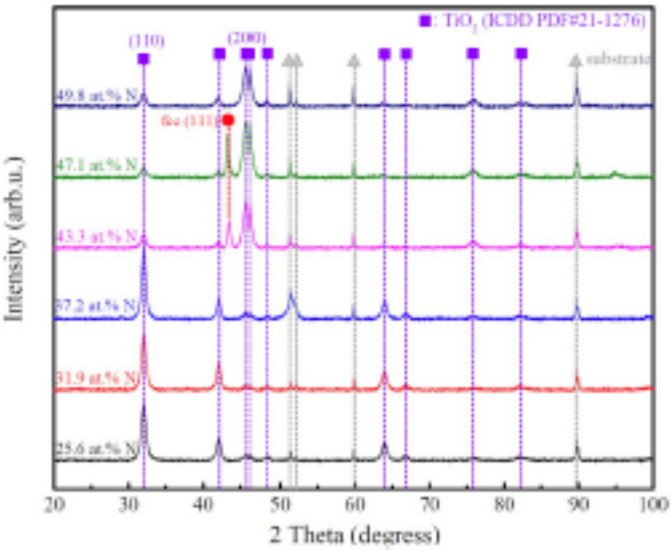
■: TiO_2 (ICDD PDF#21-1276)
(110)
(200)
substrate
fcc (111)
49.8 at.% N
47.1 at.% N
43.3 at.% N
37.2 at.% N
31.9 at.% N
25.6 at.% N
Intensity (arb.u.)
20
30
40
50
60
70
80
90
100
2 Theta (degress)

Figure 8

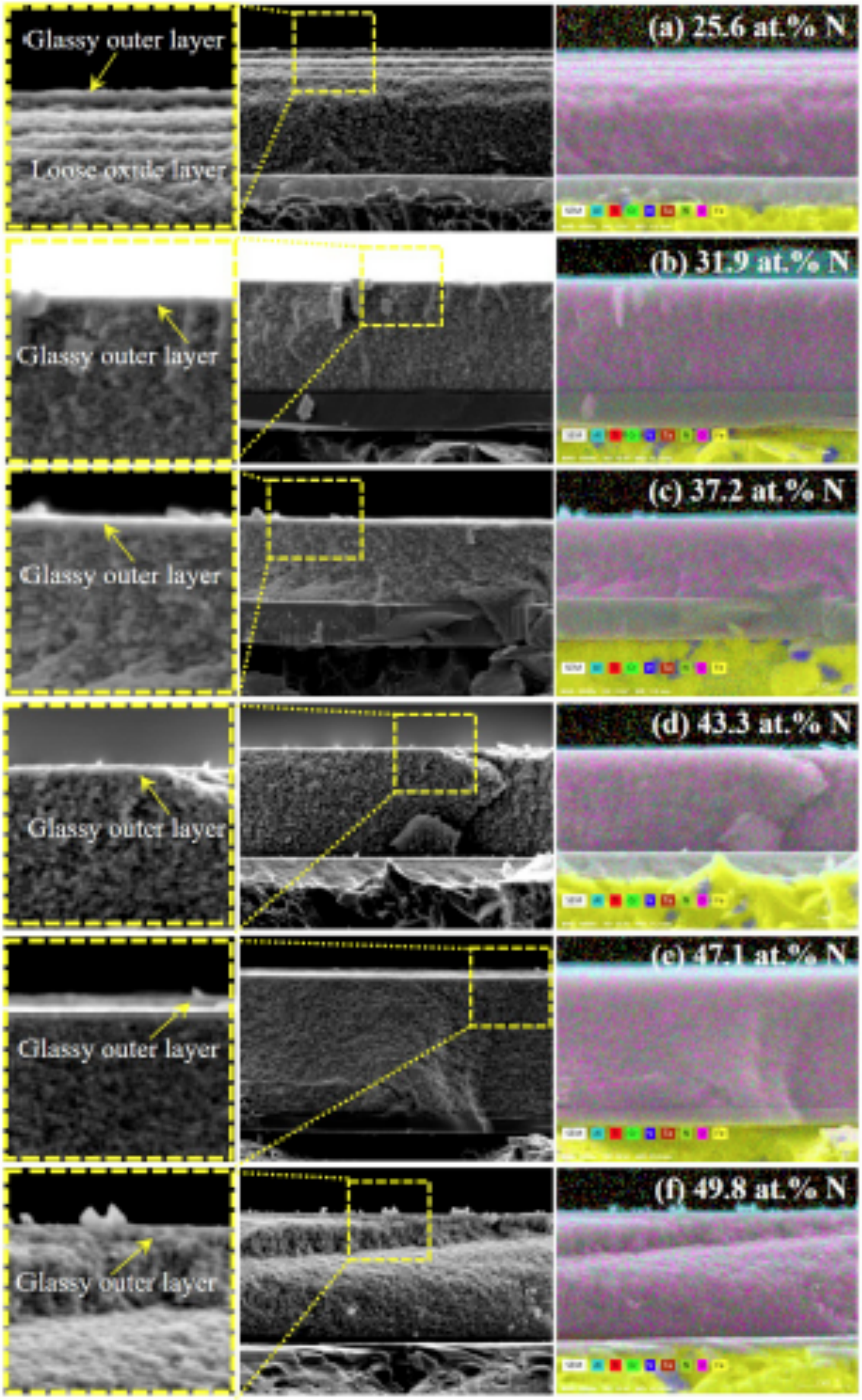
Glassy outer layer
Loose oxide layer
(a) 25.6 at.% N
Glassy outer layer
(b) 31.9 at.% N
Glassy outer layer
(c) 37.2 at.% N
Glassy outer layer
(d) 43.3 at.% N
Glassy outer layer
(e) 47.1 at.% N
Glassy outer layer
(f) 49.8 at.% N

Figure 9

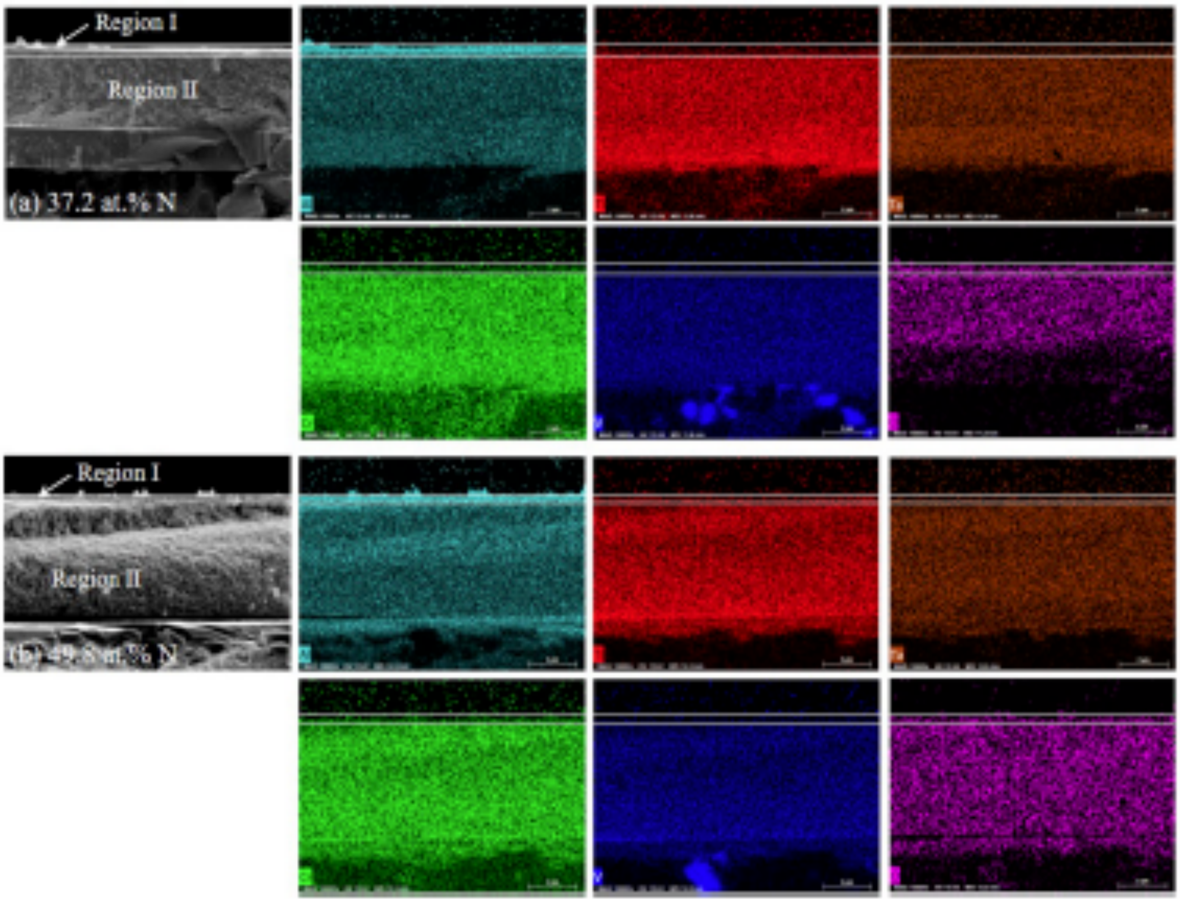

Figure 10